Acta Crystallographica Section D
Biological Crystallography
ISSN 1399-0047

Room-temperature serial crystallography at synchrotron X-ray sources using slowly flowing free-standing high-viscosity microstreams

Sabine Botha,[a] Karol Nass,[a] Thomas R. M. Barends,[a] Wolfgang Kabsch,[a] Beatrice Latz,[a] Florian Dworkowski,[b] Lutz Foucar,[a] Ezequiel Panepucci,[b] Meitian Wang,[b] Robert L. Shoeman,[a] Ilme Schlichting[a]* and R. Bruce Doak[a]*

[a]Department of Biomolecular Mechanisms, Max Planck Institute for Medical Research, Jahnstrasse 29, 69120 Heidelberg, Germany, and [b]Swiss Light Source, Paul Scherrer Institute, CH-5232 Villigen, Switzerland

Correspondence e-mail: ilme.schlichting@mpimf-heidelberg.mpg.de, bruce.doak@mpimf-heidelberg.mpg.de

Received 18 June 2014
Accepted 30 November 2014

PDB references: lysozyme, 4rlm; 4rln

Recent advances in synchrotron sources, beamline optics and detectors are driving a renaissance in room-temperature data collection. The underlying impetus is the recognition that conformational differences are observed in functionally important regions of structures determined using crystals kept at ambient as opposed to cryogenic temperature during data collection. In addition, room-temperature measurements enable time-resolved studies and eliminate the need to find suitable cryoprotectants. Since radiation damage limits the high-resolution data that can be obtained from a single crystal, especially at room temperature, data are typically collected in a serial fashion using a number of crystals to spread the total dose over the entire ensemble. Several approaches have been developed over the years to efficiently exchange crystals for room-temperature data collection. These include *in situ* collection in trays, chips and capillary mounts. Here, the use of a slowly flowing microscopic stream for crystal delivery is demonstrated, resulting in extremely high-throughput delivery of crystals into the X-ray beam. This free-stream technology, which was originally developed for serial femtosecond crystallography at X-ray free-electron lasers, is here adapted to serial crystallography at synchrotrons. By embedding the crystals in a high-viscosity carrier stream, high-resolution room-temperature studies can be conducted at atmospheric pressure using the unattenuated X-ray beam, thus permitting the analysis of small or weakly scattering crystals. The high-viscosity extrusion injector is described, as is its use to collect high-resolution serial data from native and heavy-atom-derivatized lysozyme crystals at the Swiss Light Source using less than half a milligram of protein crystals. The room-temperature serial data allow *de novo* structure determination. The crystal size used in this proof-of-principle experiment was dictated by the available flux density. However, upcoming developments in beamline optics, detectors and synchrotron sources will enable the use of true microcrystals. This high-throughput, high-dose-rate methodology provides a new route to investigating the structure and dynamics of macromolecules at ambient temperature.

1. Introduction

Radiation damage is a major limiting factor in macromolecular crystallography, particularly when using tiny crystals (Holton & Frankel, 2010) or when studying redox-active systems such as metalloproteins (Beitlich *et al.*, 2007). Since radiation damage accumulates more slowly at low temperature, crystals are conventionally held at cryogenic temperature during data collection (Garman & Schneider, 1997). While

doi:10.1107/S1399004714026327

this approach has proven to be tremendously successful in obtaining high-resolution structures, it nonetheless precludes time-resolved measurements and, more importantly, does not sample the structural distributions and dynamics present at physiological temperatures and probed biochemically in solution (Fraser *et al.*, 2011). Last but not least, room-temperature data collection eliminates the need for cryoprotectants, which can be difficult if not impossible to find, with the crystals of many viruses being prime examples. For all of these reasons, interest in room-temperature data collection has surged recently. Since radiation damage limits the amount of useful data that can be collected from a single crystal, serial data-collection approaches are typically required, merging the data from many crystals into a single data set. However, this not only requires computational methods such as clustering approaches (Foadi *et al.*, 2013; Liu, Liu *et al.*, 2013) to decide which subgroup of data to merge, but also means that damaged crystals need to be rapidly exchanged for fresh ones during data collection. A convenient way to do this is *in situ* data collection (Bingel-Erlenmeyer *et al.*, 2011; Axford *et al.*, 2012), directly exposing crystals in crystallization plates that yield very low X-ray background or in array-like crystallization platforms (Kisselman *et al.*, 2011). An added benefit of this approach is that it does not require crystal manipulation. This not only saves time but can be crucial in the case of very sensitive and fragile crystals. While *in situ* approaches are very useful for situations in which some fraction of the data can be collected from each crystal, requiring a possibly large but not huge number of crystals for a complete data set, they become inconvenient in the latter case. To this end, a chip has been developed that promotes the self-assembly of crystals into arrays by self-localization of their mother liquor to locations with favourable liquid-pinning potential (Zarrine-Afsar *et al.*, 2012). Surface modifications ensure random orientations of the crystals for efficient coverage of reciprocal space. While the X-ray background of the initial device was relatively high, the chip provides an efficient means for high-throughput data collection at both synchrotron and free-electron laser (FEL) X-ray sources, making efficient use of the sample.

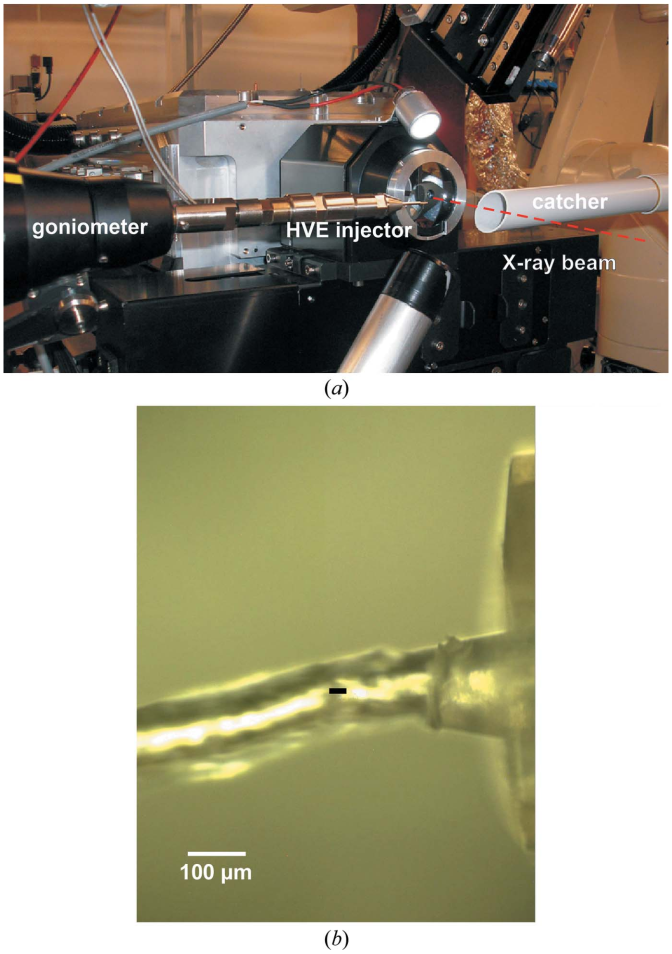

Figure 1
(*a*) HVE injector mounted on the goniometer of the PXII beamline at the SLS. (*b*) View of the extruding LCP stream. The capillary (100 µm inner diameter in this case) is shown on the right, with the LCP material flowing from right to left. The black box indicates the size (10 × 30 µm) and position of the X-ray beam.

The emerging method of serial femtosecond crystallography (SFX) at X-ray FELs allows the acquisition of high-resolution undamaged snapshot diffraction patterns at ambient temperature (Chapman *et al.*, 2011; Boutet *et al.*, 2012) by constantly supplying fresh crystals in a liquid microjet (Weierstall *et al.*, 2012, 2014; Sierra *et al.*, 2012). However, at present its use is severely limited by the available FEL beam time. Therefore, there is great interest in performing such serial room-temperature measurements at synchrotrons. A proof-of-principle measurement was performed recently at PETRA III by Chapman and coworkers, who used a pump to push a suspension of lysozyme microcrystals through a thin-walled capillary. Diffraction data were collected by moving the capillary with a continuously flowing suspension of microcrystals across the X-ray beam (Stellato *et al.*, 2014). Here, we demonstrate an alternative approach using significantly less sample by embedding the crystals in a high-viscosity medium. In addition, this approach prevents crystal settling during data collection and allows a greatly protracted exposure time at synchrotrons when compared with those at FEL sources (milliseconds *versus* femtoseconds). To this end, the crystals must pass relatively slowly through the X-ray beam while still avoiding unwanted rotations that would smear out the diffraction peaks. Our High Viscosity Extrusion (HVE) sample injector (Fig. 1, Supplementary Figs. S1 and S2) allows the extrusion of a free-standing linear stream of crystals embedded in high-viscosity media with a wide range of viscosities. Building upon previous designs (Weierstall *et al.*, 2012, 2014), the HVE injector functions both in vacuum and at atmospheric pressure and can be mounted on a standard goniometer. Owing to the continuous supply of fresh crystals, the full dose that a crystal can tolerate can be used for each single-crystal exposure, permitting the analysis of small or weakly scattering crystals, as well as those that are prone to photoreduction, such as flavoproteins (Fedorov *et al.*, 2003).

Using crystals of the model protein lysozyme embedded in a highly viscous lipidic cubic phase (LCP), we collected native serial crystallography (SX) data at wavelengths of 1.32 Å (9.4 keV) and 2.07 Å (6 keV), as well as two heavy-atom-derivative SX data sets. An anomalous difference density map calculated from the 2.07 Å wavelength SX data clearly shows the positions of the endogenous S atoms. Moreover, the heavy-atom-derivative SX data sets allowed *de novo* phasing of the structure, demonstrating the quality of the data and the usefulness of the method for biomolecular structure determination.

2. Materials and methods

2.1. Crystallization and derivatization

Native lysozyme crystals (10 × 10 × 30 and 15 × 15 × 60 µm; Supplementary Fig. S3) were grown by mixing 2.5 ml protein solution (30–60 mg ml^{-1}) with 7.5 ml precipitant solution [20%(*w*/*v*) NaCl, 6%(*w*/*v*) PEG 6000, 0.1–0.5 *M* sodium acetate pH 3.5] followed by incubation overnight at room temperature. After settling of the crystals, the crystallization solution was exchanged several times for storage solution [8%(*w*/*v*) NaCl, 0.1 *M* sodium acetate pH 4.0]. The iodide derivative was made by exchanging the storage solution for 8%(*w*/*v*) KI, 0.1 *M* sodium acetate pH 4.0. The gold derivative (Sun *et al.*, 2002) was prepared by soaking lysozyme crystals for 11 min in 15 m*M* $KAuCl_4$, 8%(*w*/*v*) NaCl, 0.1 *M* sodium acetate pH 4.6 while rotating the sample. The crystal slurry was centrifuged and washed twice with storage solution. Derivatization was apparent from the brownish colour of the crystals. Lysozyme crystals were also grown in LCP. To this end, 23 µl lysozyme solution (40 mg ml^{-1} in 50 m*M* sodium acetate buffer pH 4.5) was mixed with 39 mg monoolein from Molecular Dimensions or Sigma using a syringe mixer (Cheng *et al.*, 1998). The resulting lipidic cubic phase (LCP; ∼60 µl), which has the consistency of toothpaste, was then squirted into a 500 µl syringe filled with precipitant solution (1.6 *M* NaCl in 50 m*M* sodium acetate buffer pH 4.5), resulting in a column of lysozyme-containing LCP surrounded by precipitant solution, a setup described in Liu, Wacker *et al.* (2013). Lysozyme crystals grew inside the LCP in 24 h.

2.2. Embedding of crystals in viscous media

Lipidic cubic phase for the embedding of previously grown crystals was prepared by mixing monoolein and storage buffer, initially in a 60:40%(*w*:*v*) ratio. The amount of monoolein was then adjusted until a stable, viscous, optically isotropic phase was formed. The lysozyme crystal pellet (*e.g.* 5 µl) was gently mixed into the LCP (*e.g.* 20 µl) using coupled Hamilton syringes (Cheng *et al.*, 1998). The crystal concentration was adjusted such that mainly single-crystal hits were observed online. The crystal mixture was loaded directly from the Hamilton syringe into the injector sample reservoir using a blunt needle. The same procedure was used for embedding the crystals in other viscous media such as Vaseline. MeBiol gel was obtained from Hoelzel-Biotech.

2.3. Sample injection and SX data collection at PXII

2.3.1. Injection. After loading, the High-Viscosity Extrusion (HVE) injector (Fig. 1, Supplementary Figs. S1 and S2) was mounted on the goniometer of the PXII beamline at the Swiss Light Source (SLS). The injector piston, which is driven forward with water pumped by a Shimadzu 20AD HPLC pump, compresses a pair of Teflon balls which, driven by a pressure-amplification stage, extrude the LCP sample through a 25–100 µm inner diameter (ID) capillary (see Supplementary Fig. S1*a*). The capillary ID was chosen according to crystal size to avoid shearing and breakage of the crystals during injection, whilst being as small as possible to reduce the background contribution from the LCP stream (Supplementary Figs. S1*b* and S1*d*). A helium sheath was introduced at the point of extrusion to avoid curling up of the LCP stream. A catcher, consisting of a pipe connected to a sucking fan, was placed opposite, serving to catch the extruded sample. For the native data set collected at 1.32 Å wavelength (see below) the ID of the capillary was 40 µm, the flow rate was 21 nl min^{-1}, resulting in a driving pressure of 6500 psi (44.8 MPa), and the guiding helium-sheath gas pressure was 30 psi (2.1 MPa). The viscous matrix containing the crystals was extruded into the X-ray beam at 0.1–0.3 mm s^{-1}.

2.3.2. Native data collection. Lysozyme crystals [average sizes 10 × 10 × 30 µm (Supplementary Fig. S3) and 15 × 15 × 60 µm] embedded in a paste of LCP (see above) were extruded from a fused silica capillary at room temperature into a slow, stable stream. Native data were collected on the PXII beamline at the SLS using an unattenuated beam (2 × 10^{12} photons s^{-1} in 10 × 30 µm) and a wavelength of 1.32 Å. For still image data collection, the PILATUS 6M detector was operated in continuous shutterless mode while the stream was flowing. Diffraction patterns were recorded at 10 Hz (100 ms exposure time) and were collected in individual 'runs' of 5000 exposures. An example of a still diffraction image (native 9.4 keV data set) is shown in Supplementary Fig. S4. All diffraction patterns were saved, regardless of whether a given exposure contained a crystal hit, and were processed offline later. The recording of rotation data collection was also demonstrated (see §3.1).

2.3.3. Derivative data collection. Gold-derivative data (average crystal size 10 × 10 × 30 µm) were collected as for the native data except that 1.0 Å wavelength radiation was used (1 × 10^{12} photons s^{-1} in 10 × 30 µm). Iodide-derivative data were collected at 1.9 Å wavelength (1×10^{12} photons s^{-1} in 10 × 30 µm).

2.3.4. Sulfur anomalous signal data collection. A high-redundancy native data set was collected as stated above using 2.07 Å radiation and crystals of 15 × 15 × 60 µm in size. The use of larger crystals was necessitated by working at a longer wavelength, which resulted in a lower signal-to-noise ratio for the 10 × 10 × 30 µm crystals owing to absorption by the LCP carrier medium.

2.4. Data processing

CrystFEL (White *et al.*, 2012) was used for hit finding, peak finding and Monte Carlo integration. $R_{\rm split}$ was calculated by splitting the data into two streams consisting of even and odd run numbers (with each run containing 5000 individual

Table 1
Data processing with *CrystFEL*.

Values in parentheses are for the outer shell. n.a., not applicable; n.d., not determined.

	Native	Iodide derivative	Gold derivative	S anomalous signal
Diffraction source	PXII	PXII	PXII	PXII
Wavelength (Å)	1.32	1.9	1.0	2.07
Temperature (K)	293	293	293	293
Detector	PILATUS 6M	PILATUS 6M	PILATUS 6M	PILATUS 6M
Crystal-to-detector distance (mm)	165	180	350	165
Rotation range per image (°)	0	0	0	0
Total rotation range (°)	n.a.	n.a.	n.a.	n.a.
Exposure time per image (s)	0.1	0.1	0.1	0.1
Space group	$P4_32_12$	$P4_32_12$	$P4_32_12$	$P4_32_12$
a, b, c (Å)	78.6, 78.6, 37.9	79.2, 79.2, 37.9	79.5, 79.5, 37.8	78.6, 78.6, 37.8
α, β, γ (°)	90, 90, 90	90, 90, 90	90, 90, 90	90, 90, 90
Mosaicity (°)	n.d.	n.d.	n.d.	n.d.
Resolution range (Å)	19–1.9 (1.97–1.90)	15–2.5 (2.59–2.50)	15–2.5 (2.59–2.50)	15–2.8 (2.90–2.80)
No. of collected patterns	65000	160468	136721	349851
No. of indexed patterns	11081	42115	11915	106737
Completeness (%)	100 (100)	100 (100)	100 (100)	100 (100)
Multiplicity	527 (459)	1107 (816)	311 (225)	3085 (2226)
$\langle I/\sigma(I)\rangle$†	5.1 (1.0)	12.4 (4.4)	5.6 (1.6)	19.2 (9.1)
$R_{\rm split}$‡	0.324 (1.00)	0.259 (0.335)	0.404 (2.01)	0.063 (0.146)
CC*	0.954 (0.800)	0.923 (0.905)	0.913 (0.398)	0.996 (0.984)
$\rm CC_{ano}$	n.d.	0.391 (0.083)	0.193 (0.125)	0.227 (0.017)
Overall B factor from Wilson plot (Å^2)	42.0	47.9	45.6	37.3

† In *CrystFEL* $\langle I/\sigma(I)\rangle$ is evaluated using the $\sigma(I)$ obtained from the Monte Carlo integration, which is not the same as the conventional $\sigma(I)$. We therefore based our resolution estimates on CC*. ‡ $R_{\rm split}$ is defined in *CrystFEL* as the R factor between data sets calculated from two halves of the data, corrected for the drop in multiplicity caused by dividing the data into halves: $R_{\rm split} = (1/2^{1/2}) \sum |I^A_{hkl} - I^B_{hkl}| / \frac{1}{2} |I^A_{hkl} + I^B_{hkl}|$.

diffraction images) instead of even and odd image numbers as performed for FEL SFX data. While not an issue for the large majority of crystals used in this study, this avoids biasing the statistics in the case of larger crystals that yielded two or more consecutive diffraction images as they travelled through the X-ray beam. In addition to *CrystFEL*, the data were also processed with *nXDS* (Kabsch, 2014), which uses two-dimensional profile fitting to estimate the observed reflection intensity and for subsequent post-refinement of the correction factors relating each observation to its unique squared structure-factor amplitude.

2.5. Phasing, refinement and anomalous difference density map calculation

Phasing by multiple isomorphous replacement with anomalous scattering (MIRAS) was performed with *autoSHARP* (Vonrhein *et al.*, 2007), using the 1.32 Å wavelength data as a native data set (using data from 15 to 2.5 Å resolution) and the data from iodide-soaked and gold-soaked crystals (see above) as derivative data sets (15–2.5 Å resolution) as described in detail in §3. Refinement was performed with *REFMAC*5 (Murshudov *et al.*, 2011). The structures determined in this way using *CrystFEL* and *nXDS* data were deposited as PDB entries 4rlm and 4rln, respectively.

Molecular replacement was performed using *Phaser* 2.4.1 (McCoy *et al.*, 2007) using data between 15 and 2.5 Å resolution. PDB entry 1vds was used as the search model and the solvent content was fixed at 40%.

An anomalous difference density map was calculated using 2.07 Å wavelength lysozyme data from 15 × 15 × 60 µm crystals using phases calculated from the MIRAS structure using *Phaser* (McCoy *et al.*, 2007).

3. Results and discussion

3.1. Data collection and data analysis

We used our HVE injector to deliver lysozyme crystals embedded or grown in LCP in a free-flowing stream into the unattended X-ray beam of the PXII beamline at the SLS. Diffraction data were collected in a shutterless fashion using a PILATUS 6M detector operating at 10 Hz. The LCP-grown crystals displayed a large size distribution, and since we saw no significant difference in diffraction quality we continued with the embedded lysozyme crystals since this provides an easier way to control crystal density and to compare different carrier media. The stream was aligned such that the focus of the X-ray beam intersected the centre of the stream about 50–100 µm downstream of the nozzle exit. Visual inspection of the diffraction data from native crystals showed that ~90% of the crystals were exposed once, in accordance with expectations based on the flow rate and the good match of the X-ray focus to the crystal size.

The flow dynamics of the extruding sample stream are complicated, depending upon the nozzle geometry, the coaxial gas-flow rate and the properties of the stream itself, notably the inhomogeneity of the extrusion owing to variations in crystal density (including possible crystal aggregations) and to any inherent non-uniformity of the carrier material. We explored the influence of flow rates on the length and straightness of the stream and on the diffraction patterns for

Table 2
Data processing with *nXDS*.

Values for the outer shell are given in parentheses. n.d., not determined.

	Native	Iodide derivative	Gold derivative	S anomalous signal
Wavelength (Å)	1.32	1.9	1.0	2.07
Crystal-to-detector distance (mm)	165	180	350	165
Rotation range per image (°)	0	0	0	0
Exposure time per image (s)	0.1	0.1	0.1	0.1
Space group	$P4_32_12$	$P4_32_12$	$P4_32_12$	$P4_32_12$
a, b, c (Å)	79.0, 79.0, 38.2	79.0, 79.0, 38.2	79.1, 79.1, 37.9	79.1, 79.1, 38.1
α, β, γ (°)	90, 90, 90	90, 90, 90	90, 90, 90	90, 90, 90
Mosaicity† (°)	0.3 ± 0.1	0.2 ± 0.1	0.4 ± 0.3	0.2 ± 0.1
Resolution range (Å)	19–2.17 (2.30–2.17)	19–2.72 (2.89–2.72)	18.9–2.47 (2.62–2.49)	19.1–2.79 (2.96–2.79)
No. of patterns used	55000	184999	116679	254073
No. of indexed patterns	5190	9098	8774	49606
Completeness (%)	98.6 (96.7)	99.0 (99.3)	98.1 (93.5)	99.7 (99.7)
Multiplicity	150 (110)	119 (92)	155 (84)	682 (501)
$\langle I/\sigma(I)\rangle$‡	23.5 (9.8)	32.3 (15.5)	25.2 (6.6)	74.3 (41.6)
$\langle I/\sigma(I)\rangle_{\rm merged}$§	23	42	33	96
$\langle I/\sigma(I)\rangle_{\rm single\ measurement}$¶	1.8	2.8	1.9	2.6
$R_{\rm meas}$†† (%)	48.7 (132)	26.4 (58.1)	46.4 (184)	24.2 (40.3)
$R_{{\rm mrgd}\text{-}F}$‡‡ (%)	6.8 (21.1)	4.3 (10.5)	7.5 (38.2)	2.1 (4.4)
$CC_{1/2}$§§	99.5* (93.1*)	99.6* (97.3*)	99.6* (78.3*)	99.7* (99.2*)
$CC_{\rm ano}$§§ (%)	n.d.	74.3* (47.9*)	8.4 (5.2)	46.8* (21.7*)
Overall B factor from Wilson plot (Å^2)	31.3	26.0	46.0	21.0

† Preliminary determination of the mosaicity for each image in the INTEGRATE step of *nXDS* which is needed by the Gaussian rocking-curve determination to estimate the correction for the offset from the Ewald sphere. The method is essentially the same as that used by *XDS* (Kabsch, 2010). ‡ $\langle I/\sigma(I)\rangle$: mean of intensity $I/\sigma(I)$ of unique reflections (after merging symmetry-related observations). § $\langle I/\sigma(I)\rangle_{\rm merged}$: ⟨merged intensity/standard error(merged intensity)⟩$_{\rm merged}$. ¶ $\langle I/\sigma(I)\rangle_{\rm single\ measurement}$: ⟨intensity/standard error for a single measurement⟩$_{\rm single}$. †† Redundancy-independent R factor (on intensities). See Diederichs & Karplus (1997) for definition. ‡‡ Quality of amplitudes (F) of this data set. See Diederichs & Karplus (1997) for definition. §§ Correlation significant at the 0.1% level is marked by an asterisk (Karplus & Diederichs, 2012). $CC_{1/2}$ is the percentage of correlation between intensities from random half data sets (Karplus & Diederichs, 2012). $CC_{\rm ano}$ is the mean correlation factor between two random subsets of anomalous intensity differences.

different capillary and thus stream diameters. Higher sample-flow rates lead to an increase in the length of the contiguous extruded stream, thereby allowing the beam to intersect the stream farther downstream of the end of the capillary. The more stable stream reduces unwanted rotations of crystals owing to either actual curling of the stream or to velocity gradients within the stream. In general, the stream must be closely monitored and its speed adjusted during a measurement. Below a critical flow rate, the stream does not form a stable column but instead develops a droplet at the nozzle tip, which is then periodically blown free by the coaxial gas flow. Such a droplet increases the background scattering substantially and thus is detrimental to experimental measurements. If the flow speed is too high, crystals pass the beam too rapidly to allow reasonable diffraction intensities to be measured with the current flux density at PXII. When assembling the injector, it is important to align the inner capillary centrally in the outer sleeve, since misalignment leads to the stream curling up and and producing azimuthally streaked diffraction patterns consistent with a small rotation of the crystal around the X-ray axis (Supplementary Fig. S5).

Diffraction data were acquired in runs of 5000 exposures, which took about 10 min. The hit rate, the fraction of diffraction images containing a crystal diffraction pattern, strongly depends on the crystal concentration. For the native data set, 65 000 patterns were collected, 17 792 of which contained ≥30 Bragg peaks (hit rate 27%) and 62% of which could be indexed with *CrystFEL* (see below). Thus, acquisition of the 11 081 indexed native diffraction patterns listed in Table 1 took 2.2 h. Using a flowrate of 21 nl min^{-1}, this corresponds to ~0.3 mg protein. We also processed the data with *nXDS* (Kabsch, 2014). All indexed diffraction patterns were scaled and merged in the CORRECT step of *nXDS*. The statistics for all data sets are shown in Table 2. The results obtained by *CrystFEL* and *nXDS* processing are compared below.

Our SX approach not only allows the collection of stills ($\Delta\varphi$ = 0°) but also of rotation data by rotating the injector around the φ axis during data collection. For the acquisition of rotation data the injector was rotated by $+\Delta\varphi$ (*e.g.* 0.3°) around the spindle axis during the 100 ms exposure, similarly as for a regular rotation exposure. The injector was then rotated back quickly by $-\Delta\varphi$ (*e.g.* −0.3°), since extended unidirectional rotation was precluded by the gas and liquid supply lines attached to the injector. After a waiting period of 1 s another rotation image was collected, repeating the sequence. Without such a waiting period rotational smearing of the reflections was observed (see Supplementary Fig. S5), which was due to a persisting rotational quivering of the stream induced by the fast ($-\Delta\varphi$) back-rotation, which would otherwise continue through the 100 ms acquisition period of the PILATUS detector. A comparison of still *versus* rotational data will be published elsewhere. Higher flux density, correspondingly reduced exposure times and faster detectors will obviate the need for this wait time, allowing fully shutterless operation.

The advantage of using lysozyme as a model system for methods development is that it allows the comparison of data collected using different approaches. Boutet and coworkers compared SFX data from lysozyme microcrystals with low-

Table 3
Molecular-replacement results.

	RFZ†	TFZ‡	LLG after rigid-body refinement
CrystFEL (this study)	14.7	35.1	1460
nXDS (this study)	14.7	36.4	1406
Data from Stellato *et al.* (2014)	14.8	35.8	1301
40 fs FEL (Boutet *et al.*, 2012)	13.8	34.8	1002
5 fs FEL (Boutet *et al.*, 2012)	14.4	34.0	1024
24 kGy synchrotron data (Boutet *et al.*, 2012)	14.2	34.8	1037

† Rotation-function *Z*-score. ‡ Translation-function *Z*-score.

Table 4
Structure solution and refinement.

Values in parentheses are for the outer shell.

	Native, *CrystFEL*	Native, *nXDS*	Stellato *et al.* (2014), re-refinement†
Resolution range (Å)	19–1.9 (1.95–1.90)	18–2.2 (2.22–2.17)	56–2.1 (2.15–2.09)
Completeness (%)	100 (100)	99.1 (100)	93.4 (82.0)
σ Cutoff	None	None	None
No. of reflections			
Working set	9320	6399	6775
Test set	477	328	345
Final $R_{\rm cryst}$	0.196 (0.300)	0.193 (0.233)	0.191 (0.303)
Final $R_{\rm free}$	0.243 (0.279)	0.238 (0.348)	0.246 (0.335)
Cruickshank DPI	0.170	0.291	0.262
No. of non-H atoms			
Protein	1001	1001	1001
Water	30	38	40
Total	1031	1039	1041
R.m.s. deviations			
Bonds (Å)	0.008	0.007	0.007
Angles (°)	1.169	1.143	0.125
Average *B* factors (Å^2)			
Protein	48.0	23.4	47.5
Water	52.6	27.0	47.7
Ramachandran plot (%)			
Most favoured	96.8	97.6	97.6
Allowed	3.2	2.4	2.4

† For a better comparison of the statistics, we re-refined against the data from Stellato *et al.* (2014) using the same protocol as for the other data sets.

Table 5
SIRAS results for the iodide derivative.

Statistics were calculated by *SHARP* (Vonrhein *et al.*, 2007).

	FOM†		PP$_{\rm iso}$‡		PP$_{\rm ano}$‡	
	Acentric	Centric	Acentric	Centric	Acentric	Centric
nXDS	0.44	0.36	1.434	1.025	1.431	
CrystFEL	0.47	0.44	1.800	1.351	1.042	

† FOM is the figure of merit. ‡ PP$_{\rm iso}$ and PP$_{\rm ano}$ are the isomorphous and anomalous phasing power, respectively.

Table 6
MIRAS results.

Statistics were calculated by *SHARP* (Vonrhein *et al.*, 2007).

			Iodide derivative			Gold derivative		
	FOM		PP$_{\rm iso}$			PP$_{\rm iso}$		
	Acentric	Centric	Acentric	Centric	PP$_{\rm ano}$	Acentric	Centric	PP$_{\rm ano}$
nXDS	0.44	0.38	1.438	1.043	1.077	0.271	0.213	0.224
CrystFEL	0.49	0.47	1.748	1.318	1.039	0.565	0.471	0.244

dose rotation data collected using synchrotron radiation from similarly grown macroscopic lysozyme crystals kept at room temperature and concluded that there is reasonable agreement between the data and no indication of radiation damage, thereby validating the novel SFX approach for data acquisition (Boutet *et al.*, 2012). With the same motivation, and inspired by the recent comments made by Rossmann (2014), we compared our SX data collected with the high-extrusion injector with the data collected by SFX (Boutet *et al.*, 2012), low-dose room-temperature synchrotron data (Boutet *et al.*, 2012) and the SX data collected by Stellato and coworkers using a flowing stream in a capillary for crystal delivery (Stellato *et al.*, 2014).

Regardless of the program used for processing, the low-resolution data range showed poor statistics. This could be owing to background scatter from the LCP carrier medium; however, this decrease in low-resolution data quality is also frequently observed for SFX data (see, for example, Boutet *et al.*, 2012). We therefore applied a low-resolution cutoff at 15 Å for the molecular-replacement (MR) calculations. MR using these data sets resulted in very similar rotation-function and translation-function *Z*-scores (see Table 3). Also, refinement of a lysozyme model against these data sets resulted in very similar *R* factors and geometries, as can be seen in Table 4. The only difference between the results obtained with the various data sets is in the Wilson *B* factors and the individual *B* factors after refinement, which are significantly higher for the data sets processed using *CrystFEL* [37–47 Å^2 for *CrystFEL* data (Table 1) *versus* 21–46 Å^2 for *nXDS* data (Table 2)]. This is probably owing to *CrystFEL* using a global resolution cutoff for all images, which results in the addition of very weak data or even noise at higher resolution. This is reflected in the lower signal-to-noise ratio at high resolution for data processed using *CrystFEL* (see below).

3.2. Phasing and anomalous signals

To investigate the quality of the data and to establish the usefulness of SX as a standalone method for structure determination, phasing by multiple isomorphous replacement with anomalous scattering was performed using *autoSHARP* (Vonrhein *et al.*, 2007), using the 1.32 Å wavelength data as a native data set (using data to 2.5 Å resolution) and the data from iodide-soaked and gold-soaked crystals (see above) as derivative data sets.

Initially, four iodide sites were found using isomorphous differences using the *CrystFEL* data. *SHARP* then refined these sites, found two additional sites and calculated phases using data to 3.5 Å resolution. These phases were used to identify the single gold-binding site. Using these sites, we compared phasing by SIRAS and MIRAS using either *CrystFEL*-processed or *nXDS*-processed data.

FOMs and phasing power statistics are given in Tables 5 and 6. Supplementary Fig. S6 shows the anomalous signal-to-noise ratios for the two derivatives for both programs. When performing SIRAS using only the iodide derivative, both *CrystFEL*-processed and *nXDS*-processed data resulted in an interpretable map. However, the *nXDS* data allowed an almost complete model to be automatically built by *ARP/wARP* (Langer *et al.*, 2008), whereas for the *CrystFEL* data only about 50% of the structure could be built automatically. MIRAS using both the iodide and gold derivatives was also successful in both cases, but here too the *nXDS* data resulted in a more complete model being built more rapidly. Importantly, the FOMs and phasing powers were generally higher when the data from *CrystFEL* were being used. However, even for the *CrystFEL* data the phasing powers generally dropped dramatically at resolutions better than 3 Å. These relatively poor phasing powers below 3 Å are likely to be owing to nonisomorphism between the native and derivative data sets rather than to poor data quality, given the good phasing powers at lower resolution. At very low resolution (worse than 9 Å), however, the phasing powers drop significantly. Such a drop at low resolution is not, however, present in the FOM statistics.

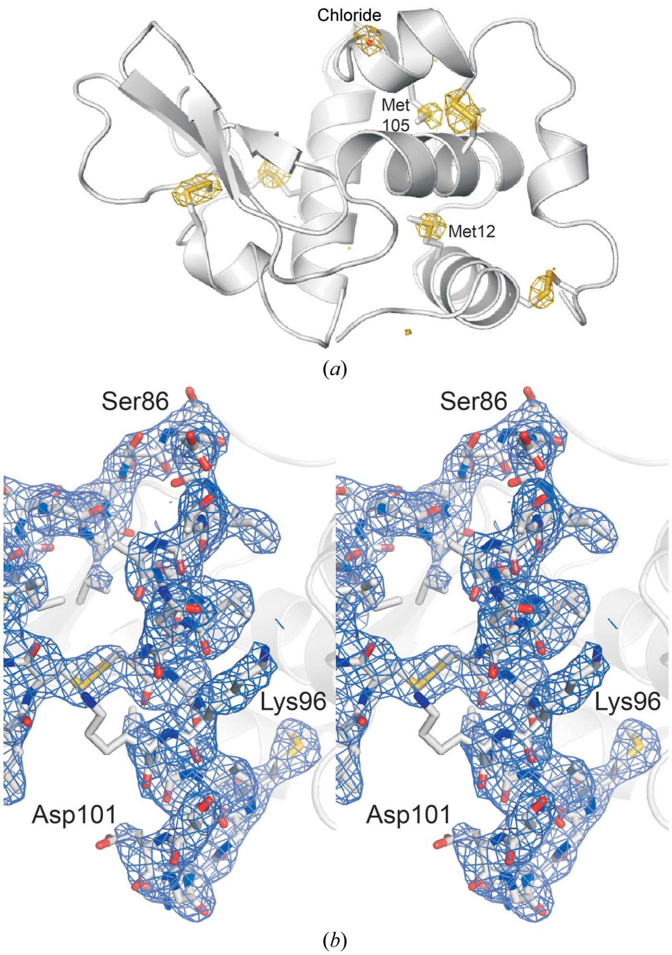

Figure 2
(*a*) Anomalous difference density map contoured at 3.5σ, calculated from SX data to 2.8 Å resolution using molecular-replacement phases, showing the S atoms in lysozyme as well as a possible chloride ion (red sphere). (*b*) Stereofigure showing part of the MIRAS map calculated using SX data processed with *CrystFEL* to 2.5 Å resolution after solvent flattening. The map is contoured at 1σ and overlaid on the final refined structure.

It is possible that the inclusion of more data by *CrystFEL* has increased the usefulness of the *CrystFEL* data for phasing, whereas the more conventional intensity distributions of the *nXDS*-processed data (Supplementary Fig. S7) made them more amenable to automatic building. This underlines once again how data collection and processing need to be tailored to the goal of the experiment: for experimental phasing far more accurate structure-factor amplitudes are required than for molecular replacement or for difference density map calculations. For serial crystallography, this translates directly into the number of images needed for experimental phasing being far higher than for other needs.

To further assess the quality of the SX data, we investigated the anomalous signal of the endogenous S atoms (Fig. 2*a*) in the data collected at 2.07 Å wavelength. Indeed, an anomalous difference density map calculated from *CrystFEL* data shows peaks of >5σ at the positions of all of the S atoms in lysozyme, as well as at the position of a putative chloride ion. This is the first step towards sulfur-SAD phasing from SX data.

3.3. *CrystFEL versus nXDS*

As shown above, both data-processing programs delivered data of largely comparable quality, with differences in the Wilson *B* factors (Tables 1 and 2) and cumulative intensity distributions (Supplementary Fig. S7) that are likely to be caused by the different approaches to determining the resolution. The overall agreement of the data is remarkable, given that the data sets processed by *nXDS* included far fewer images than those processed by *CrystFEL* (see Tables 1 and 2), since the *nXDS* version used in this study did not index as many images as *CrystFEL*. *CrystFEL* is based on Monte Carlo integration (Kirian *et al.*, 2010), which depends crucially on the averaging of large numbers of measurements, whereas *nXDS* uses explicit forms for each reflection relating the recorded intensity in each image pixel to the corresponding unique squared structure-factor amplitude (Kabsch, 2014).

Another important difference between data from *CrystFEL* and *nXDS* is in the determination of errors. *CrystFEL* uses the standard deviation of the set of measurements that is averaged to obtain a unique intensity as the standard error of that intensity. *nXDS*, on the other hand, determines the standard error of an intensity as recorded in each still image in the same way as in the conventional rotation data-processing program *XDS* (Kabsch, 2010). In both *nXDS* and *XDS* it is assumed that the contents of each detector pixel are proportional to a Poisson distribution. The initial standard error is then inflated in the CORRECT step later on to be consistent with sampling statistics of the intensities of all symmetry-related reflections in the whole data set.

This difference complicates the comparison of signal-to-noise ratios from the two programs.

The fact that comparable data can be obtained using *nXDS* from far fewer images illustrates the effectiveness of the *nXDS* approach. Further improvement of the indexing routines in *nXDS* allowing more images to be included may therefore be expected to lead to large improvements in data quality as well

Table 7
Illustrative flow parameters as computed to collect 50 000 indexed diffraction patterns at an indexing rate of 20% for 100 ms X-ray exposures in 'shutterless' mode with an X-ray footprint of 10 × 30 µm (across by along sample stream) and a single-crystal hit probability of 67% in the intersection volume of the X-ray beam and the sample stream.

The density of the crystalline material is taken to be 1.3 mg cm^{-3}. A tool for the calculation of these numbers has been provided in the Supporting Information.

Diameter of sample stream (µm)	Crystal length along stream (µm)	Stream flow speed (mm s^{-1})	Solution density (crystals ml^{-1})	Total sample volume required (µl)	Total crystal mass required (µg)	Geometrical efficiency of beam–stream intersection	Time required for 50 000 patterns (h)
25	1	0.47	9.1×10^7	17	2	0.50	20
25	5	0.53	9.1×10^7	17	256	0.50	18
25	10	0.60	9.1×10^7	17	512	0.50	16
50	1	0.47	4.5×10^7	131	8	0.25	40
50	5	0.53	4.5×10^7	131	982	0.25	35
50	10	0.60	4.5×10^7	131	1964	0.25	31
100	1	0.47	2.2×10^7	1043	31	0.13	79
100	5	0.53	2.2×10^7	1043	3888	0.13	70
100	10	0.60	2.2×10^7	1043	7775	0.13	61

as to a large reduction in the total number of images and therefore the sample and beam time required for a full data set.

3.4. The injection medium

Our SX approach relies on a viscous, slowly extruding carrier medium. Use of LCP is most advantageous when the biomolecule of interest is crystallized directly inside the LCP. For measurements performed at ambient temperature, as in the present instance, there is no need to use lipids with low phase-transition temperatures (such as 7.7 MAG), as is the case for FEL measurements performed in vacuum (Liu, Wacker *et al.*, 2013; Weierstall *et al.*, 2014). However, a large range of widely used crystallization conditions, such as for instance high concentrations of ammonium sulfate, are incompatible with standard LCPs. Successful embedding of solution-grown crystals into LCP therefore requires careful testing in each specific instance. Thus, to increase the applicability of SX, we searched for alternative carrier media.

Viable carrier media must combine chemical compatibility with a broad range of biomolecules, and the chemical composition of their crystallization solutions, with adjustable, but still high, viscosity, ease of embedding crystals without damaging them, low X-ray background and flow properties commensurate with a stable stream of the desired stream diameter and speed. We have identified several compounds that meet these requirements and form a stable, slowly flowing stream when discharged from our high-viscosity extrusion injector. These include hydrocarbons such as Vaseline (petroleum jelly) and block polymers such as Mebiol gel, a thermoreversibly gelling polymer that can also be used for crystallization (Sugiyama *et al.*, 2013). An analysis of the background scattering from LCP and Vaseline under the same experimental conditions is included in the Supporting Information (§S2 and Supplementary Fig. S8).

The minimum possible sample consumption in these synchrotron experiments is ultimately fixed by the requirement that a crystal in the sample free stream not be hit more than once by the X-ray beam. The flow speed of the sample stream is then set simply by the length of the crystals along the stream and the length of time during which the shutter is open. This flow speed, along with the diameter of the beam, fixes the volumetric flow rate of the sample solution. The concentration of crystals in the sample solution is chosen to give a desired probability of a single crystal being within the intersection volume between the X-ray beam and sample stream during an X-ray pulse. From this, and knowing the number of indexed diffraction patterns to be collected plus the indexing rate, the measurement time and the required amount of sample can be computed. These various inputs and outputs are easily assembled on a spreadsheet, with appropriate 'if' statements to incorporate different cases of scattering geometry (transverse dimension of X-ray larger than the X-ray beam diameter or *vice versa*). A table of flow parameters calculated in this fashion is presented in Table 7, compiled using the spreadsheet included in the Supporting Information. Should considerations other than sample consumption pose the dominant experimental limitation, these results would need to be scaled appropriately. If radiation damage is the limiting factor, for example, exposure times would need to be reduced or the flow rate increased at the expense of added sample consumption and lower diffraction intensity. Likewise, if signal to background is the primary experimental concern, then the ratio of crystal size to stream diameter becomes the dominant issue. In general, the crystal size should be matched as closely as possible to the stream diameter.

For 25–50 µm diameter sample streams, it is seen that no more than a few tens of microlitres of sample solution are required to record 50 000 indexed diffraction patterns, with the solution at a high but not unreasonable crystal density and flowing at a fraction of a millimetre per second. This crystal density (10^8 crystals ml^{-1} or less) reflects only viable crystals; if some fraction of the total number of crystals do not diffract the required crystal density will be proportionally higher. This number of diffraction patterns could be recorded in one to several 8 h shifts while consuming at most about 1 mg in total (or even much less) of crystalline material (crystals of 1–10 µm in size; for this size, the flow speed is determined largely by the assumed 30 µm extent of the X-ray footprint along the sample stream). With a 100 µm diameter stream, sample consumption increases significantly owing to the larger mismatch between the X-ray footprint and the sample stream. X-ray background owing to scattering from the stream material rises considerably, but for sufficiently large crystals, for example those approaching the stream diameter in size, the ratio of signal to background may actually be favourable.

3.5. Serial crystallography at synchrotron X-ray sources

Merging the diffraction data from dozens or even hundreds of crystals is not uncommon in virus crystallography (Grimes *et al.*, 1998; Nakagawa *et al.*, 2003; Abrescia *et al.*, 2004; Wang *et al.*, 2012). Often virus crystals cannot be cryocooled, which limits the amount of useable data that can be collected from an individual crystal, necessitating serial approaches. Data collection at FELs in the diffraction-before-diffraction regime requires very fast and efficient crystal replacement since each individual crystal is destroyed by a single exposure and data from a fresh crystal can be acquired at 120 Hz, the repetition rate of the X-ray pulses at the LCLS and the detector framing rate. This required the development of high-throughput sample-delivery systems that include chips (Zarrine-Afsar *et al.*, 2012) and different forms of liquid microjets (Weierstall *et al.*, 2012, 2014; Sierra *et al.*, 2012). Given the advantages of room-temperature data collection and recent developments for increasing the photon flux density and in detector technology, there is a growing interest in porting SFX approaches to synchrotrons for room-temperature SX. Recently, Stellato *et al.* (2014) described a setup consisting of a 100 µm inner diameter glass capillary with 10 µm thick walls that is moved axially through the X-ray beam while a suspension of microcrystals is pushed through the capillary. The capillary movement is needed to avoid the accumulation of material on the wall of the capillary in the irradiated region. In contrast, our HVE injector enables data collection using a free-flowing stream of injection medium without a capillary surrounding the sample, eliminating any X-ray scattering from such a capillary. Moreover, depending on the viscosity of the carrier medium, the stream diameter can be decreased significantly, again reducing background scattering (see §S3). The high viscosity of the carrier medium not only eliminates the problem of crystal settling observed in liquids (Lomb *et al.*, 2012; Stellato *et al.*, 2014) but most importantly it significantly reduces the flow rate and thus the sample consumption. To collect 1 500 000 diffraction patterns in 17 h, ~40 000 of which could be indexed, Stellato and coworkers used 250 mg of lysozyme, whereas we used ~0.3 mg in 2.2 h to collect 65 000 diffraction patterns, ~11 000 of which could be indexed.

Radiation damage is a serious issue and a potential limitation of macromolecular crystallography, in particular for room-temperature data collection. Following the initial photoionization events and the ensuing electron cascades (Nave & Hill, 2005), a variety of radical reactions take place that differ in their timescales and temperature-dependence. The generated electrons react very rapidly with the sample, in particular with the ubiquitous water molecules, producing, for example, hydrated electrons and hydroxyl radicals. The electrons also react with the crystallized macromolecule, resulting in the breakage of covalent bonds *etc.* The ensuing processes are slower and temperature-dependent, involving diffusion of radicals, resulting in additional bond breakages, and on even longer time scales larger structural disorder and relaxation take place. This results in both local and global damage that changes the electronic and chemical properties of the crystallized molecule itself as well as its arrangement in the lattice, which often results in an increase in mosaicity and temperature factors and decrease in high-resolution diffraction. FEL-based femtosecond data acquisition allows all but the primary radiation-damage processes to be outrun and is therefore the method of choice to collect undamaged data from highly radiation-sensitive systems. This includes the recent demonstration of a peroxide ligand in the fully 'oxidized resting fast' state of cytochrome *c* oxidase (Hirata *et al.*, 2014) and the undamaged oxygen-evolving complex of photosystem II (Kern *et al.*, 2013).

Importantly, it has recently become apparent that radiation damage can also be outrun at synchrotrons when collecting diffraction data from crystals kept at ambient temperature because then, in contrast to data collection using cryocooled crystals, the damage response is dose-rate-dependent (Owen *et al.*, 2012; Warkentin *et al.*, 2013). It has been shown that the lifetime of crystals can be significantly prolonged if the data are collected with a high dose rate. The likely reason for a lag phase of several tens of milliseconds before the onset of radiation damage is rooted in radical quenching within and diffusion through the solvent (Owen *et al.*, 2012). This suggests that crystal lifetimes can be increased significantly for very high dose-rate data collection, which can be achieved by high flux densities in combination with very fast detectors. Essential for this approach will be an efficient system for crystal delivery such as that described here. Whether this approach will also allow the collection of undamaged data from redox-sensitive systems remains to be seen, however. Metal centres will likely be photoreduced owing to their high absorption cross-sections or be modified otherwise by photoelectrons or Auger electrons, resulting in a much lower tolerable dose on the order of just kilograys at cryogenic temperature (Beitlich *et al.*, 2007). Of importance will be to what extent recombination reactions take place during X-ray exposure. In this context it is of interest to note that an intact bond between the active-site cysteine and the flavin cofactor was observed in the room-temperature structure of a reaction intermediate of the LOV photoreceptor domain (Crosson & Moffat, 2002), but not in the cryo structure (Fedorov *et al.*, 2003) unless composite (serial) data-collection approaches were used. Presumably, the radiolysed intermediate recombined at room temperature but not at cryogenic temperature. Both structures showed a distorted flavin consistent with adduct formation.

4. Outlook and conclusions

Here, we describe proof-of-principle, high-throughput, room-temperature SX experiments at a synchrotron beamline using lysozyme as a well established model system to test a new high-viscosity extrusion injector. Use of a stream for crystal delivery allows very rapid crystal exchange, permitting a maximally tolerable dose to be administered per crystal and exposure, with the magnitude of this dose strongly depending on the specific system and the experimental objective. The use of a crystal carrier medium with a high and adjustable viscosity not only affords appropriate temporal overlap between a moving crystal and X-ray beam commensurate with required exposure times but also minimizes sample consumption. In the current experiment we used relatively large crystals, as dictated by the available X-ray flux density. Nevertheless, much less than one milligram of protein sufficed to collect a full, high-resolution SX data set. Admittedly, a few cryocooled crystals of this size could give an excellent low-dose rotation data set. Even room-temperature measurements are possible with such crystals, albeit significantly more difficult owing to the strongly reduced tolerable dose, which requires large-scale crystal exchange. The utility of the high-viscosity extrusion SX technique becomes pronounced, however, in room-temperature measurements on true microcrystals, which necessitate high-throughput sample exchange, similarly to FEL SFX experiments. Such measurements will require higher flux densities and detectors with faster framing rates, as recently explored by Stellato and coworkers at PETRA III. SX measurements of microcrystals will also require thinner streams to decrease the background. Our HVE injector can handle a wide range of viscosities and we have identified materials other than LCP that can be used as suitable carrier media, either alone or in combination. By showing that the SX data are of reasonable quality, allowing *de novo* phasing, we demonstrate the accuracy of the data and thus the usefulness of the method for data collection. Despite the need to use relatively large crystals in these seminal measurements, less than a half a milligram of protein sufficed to collect a SX data set. This amount will decrease significantly when using smaller crystals.

Beyond simply demonstrating the current feasibility of the SX method, this work suggests a possible extension of the technique to experimental capabilities that are not currently available. Time-resolved pump–probe measurements to study light-induced reactions, for example, could easily be incorporated into this scheme. In addition, we expect the impact of serial crystallography at synchrotrons to increase dramatically with the upcoming new generations of detectors such as EIGER (Dinapoli *et al.*, 2013). Developments at synchrotron facilities (such as the use of pink beams), as well as advances in the synchrotrons themselves (such as the commissioning of diffraction-limited storage rings; see the September 2014 issue of the *Journal of Synchrotron Radiation*), will increase the frame rates and flux by one to two orders of magnitude. This not only makes better use of sample and beamtime, but also allows the investigation of much smaller crystals, as is in fact ideal for high-viscosity SX measurements.

Note added in proof. The injector can also be mounted perpendicular to the spindle axis using a bracket. This has the advantage that gravity provides additional stability to the vertically extruding jet (see Supplementary Fig. S9). Recently, Sugahara *et al.* (2015) described a grease matrix as a versatile carrier medium that also works well in our HVE injector.

5. Related literature

The following references are cited in the Supporting Information for this article: Barends et al. (2014), Weiss (2001), Weiss *et al.* (2001) and Zeldin *et al.* (2013).

We thank James Holton at LBL for fruitful discussions and for performing the calculations of background signals. Portions of this research were carried out at the Swiss Light Source of the Paul Scherrer Institute, Villigen, Switzerland. We acknowledge support from the Max Planck Society and from the European Union through Marie Curie Incoming International Fellowship Grant 298405 to RBD. We thank our machine shop for their excellent work in fabricating the injectors employed in these measurements and the staff at the SLS for their support, and we are grateful to Chris Roome and Frank Koeck for outstanding computing support.

References

Abrescia, N. G. A., Cockburn, J. J. B., Grimes, J. M., Sutton, G. C., Diprose, J. M., Butcher, S. J., Fuller, S. D., San Martín, C., Burnett, R. M., Stuart, D. I., Bamford, D. H. & Bamford, J. K. H. (2004). *Nature (London)*, **432**, 68–74.

Axford, D. *et al.* (2012). *Acta Cryst.* D**68**, 592–600.

Barends, T. R. M., Foucar, L., Botha, S., Doak, R. B., Shoeman, R. L., Nass, K., Koglin, J. E., Williams, G. J., Boutet, S., Messerschmidt, M. & Schlichting, I. (2014). *Nature (London)*, **505**, 244–247.

Beitlich, T., Kühnel, K., Schulze-Briese, C., Shoeman, R. L. & Schlichting, I. (2007). *J. Synchrotron Rad.* **14**, 11–23.

Bingel-Erlenmeyer, R., Olieric, V., Grimshaw, J. P. A., Gabadinho, J., Wang, X., Ebner, S. G., Isenegger, A., Schneider, R., Schneider, J., Glettig, W., Pradervand, C., Panepucci, E. H., Tomizaki, T., Wang, M. & Schulze-Briese, C. (2011). *Cryst. Growth Des.* **11**, 916–923.

Boutet, S. *et al.* (2012). *Science*, **337**, 362–364.

Chapman, H. N. *et al.* (2011). *Nature (London)*, **470**, 73–77.

Cheng, A., Hummel, B., Qiu, H. & Caffrey, M. (1998). *Chem. Phys. Lipids*, **95**, 11–21.

Crosson, S. & Moffat, K. (2002). *Plant Cell*, **14**, 1067–1075.

Diederichs, K. & Karplus, P. A. (1997). *Nature Struct. Mol. Biol.* **4**, 269–275.

Dinapoli, R., Bergamaschi, A., Greiffenberg, D., Henrich, B., Horisberger, R., Johnson, I., Mozzanica, A., Radicci, V., Schmitt, B., Shi, X. & Tinti, G. (2013). *Nucl. Instrum. Methods Phys. Res. A*, **731**, 68–73.

Fedorov, R., Schlichting, I., Hartmann, E., Domratcheva, T., Fuhrmann, M. & Hegemann, P. (2003). *Biophys. J.* **84**, 2474–2482.

Foadi, J., Aller, P., Alguel, Y., Cameron, A., Axford, D., Owen, R. L., Armour, W., Waterman, D. G., Iwata, S. & Evans, G. (2013). *Acta Cryst.* D**69**, 1617–1632.

Fraser, J. S., van den Bedem, H., Samelson, A. J., Lang, P. T., Holton, J. M., Echols, N. & Alber, T. (2011). *Proc. Natl Acad. Sci. USA*, **108**, 16247–16252.

Garman, E. F. & Schneider, T. R. (1997). *J. Appl. Cryst.* **30**, 211–237.

Grimes, J. M., Burroughs, J. N., Gouet, P., Diprose, J. M., Malby, R., Zientara, S., Mertens, P. P. C. & Stuart, D. I. (1998). *Nature (London)*, **395**, 470–478.

Hirata, K. *et al.* (2014). *Nature Methods*, **11**, 734–736.

Holton, J. M. & Frankel, K. A. (2010). *Acta Cryst.* D**66**, 393–408.

Kabsch, W. (2010). *Acta Cryst.* D**66**, 125–132.

Kabsch, W. (2014). *Acta Cryst.* D**70**, 2204–2216.

Karplus, P. A. & Diederichs, K. (2012). *Science*, **336**, 1030–1033.
Kern, J. *et al.* (2013). *Science*, **340**, 491–495.
Kirian, R. A., Wang, X., Weierstall, U., Schmidt, K. E., Spence, J. C. H., Hunter, M., Fromme, P., White, T., Chapman, H. N. & Holton, J. (2010). *Opt. Express*, **18**, 5713–5723.
Kisselman, G., Qiu, W., Romanov, V., Thompson, C. M., Lam, R., Battaile, K. P., Pai, E. F. & Chirgadze, N. Y. (2011). *Acta Cryst.* D**67**, 533–539.
Langer, G., Cohen, S. X., Lamzin, V. S. & Perrakis, A. (2008). *Nature Protoc.* **3**, 1171–1179.
Liu, Q., Liu, Q. & Hendrickson, W. A. (2013). *Acta Cryst.* D**69**, 1314–1332.
Liu, W., Wacker, D. *et al.* (2013). *Science*, **342**, 1521–1524.
Lomb, L., Steinbrener, J., Bari, S., Beisel, D., Berndt, D., Kieser, C., Lukat, M., Neef, N. & Shoeman, R. L. (2012). *J. Appl. Cryst.* **45**, 674–678.
McCoy, A. J., Grosse-Kunstleve, R. W., Adams, P. D., Winn, M. D., Storoni, L. C. & Read, R. J. (2007). *J. Appl. Cryst.* **40**, 658–674.
Murshudov, G. N., Skubák, P., Lebedev, A. A., Pannu, N. S., Steiner, R. A., Nicholls, R. A., Winn, M. D., Long, F. & Vagin, A. A. (2011). *Acta Cryst.* D**67**, 355–367.
Nakagawa, A., Miyazaki, N., Taka, J., Naitow, H., Ogawa, A., Fujimoto, Z., Mizuno, H., Higashi, T., Watanabe, Y., Omura, T., Cheng, R. H. & Tsukihara, T. (2003). *Structure*, **11**, 1227–1238.
Nave, C. & Hill, M. A. (2005). *J. Synchrotron Rad.* **12**, 299–303.
Owen, R. L., Axford, D., Nettleship, J. E., Owens, R. J., Robinson, J. I., Morgan, A. W., Doré, A. S., Lebon, G., Tate, C. G., Fry, E. E., Ren, J., Stuart, D. I. & Evans, G. (2012). *Acta Cryst.* D**68**, 810–818.
Rossmann, M. G. (2014). *IUCrJ*, **1**, 84–86.
Sierra, R. G. *et al.* (2012). *Acta Cryst.* D**68**, 1584–1587.
Stellato, F. *et al.* (2014). *IUCrJ*, **1**, 204–212.
Sugahara, M. *et al.* (2015). *Nat. Methods* **12**, 61–63.
Sugiyama, S., Shimizu, N., Sazaki, G., Hirose, M., Takahashi, Y., Maruyama, M., Matsumura, H., Adachi, H., Takano, K., Murakami, S., Inoue, T. & Mori, Y. (2013). *Cryst. Growth Des.* **13**, 1899–1904.
Sun, P. D., Radaev, S. & Kattah, M. (2002). *Acta Cryst.* D**58**, 1092–1098.
Vonrhein, C., Blanc, E., Roversi, P. & Bricogne, G. (2007). *Methods Mol. Biol.* **364**, 215–230.
Wang, X. *et al.* (2012). *Nature Struct. Mol. Biol.* **19**, 424–429.
Warkentin, M., Hopkins, J. B., Badeau, R., Mulichak, A. M., Keefe, L. J. & Thorne, R. E. (2013). *J. Synchrotron Rad.* **20**, 7–13.
Weierstall, U. *et al.* (2014). *Nature Commun.* **5**, 3309.
Weierstall, U., Spence, J. C. H. & Doak, R. B. (2012). *Rev. Sci. Instrum.* **83**, 035108.
Weiss, M. S. (2001). *J. Appl. Cryst.* **34**, 130–135.
Weiss, M. S., Sicker, T. & Hilgenfeld, R. (2001). *Structure*, **9**, 771–777.
White, T. A., Kirian, R. A., Martin, A. V., Aquila, A., Nass, K., Barty, A. & Chapman, H. N. (2012). *J. Appl. Cryst.* **45**, 335–341.
Zarrine-Afsar, A., Barends, T. R. M., Müller, C., Fuchs, M. R., Lomb, L., Schlichting, I. & Miller, R. J. D. (2012). *Acta Cryst.* D**68**, 321–323.
Zeldin, O. B., Gerstel, M. & Garman, E. F. (2013). *J. Appl. Cryst.* **46**, 1225–1230.